ELSEVIER

Journal of Nuclear Materials 304 (2002) 221–236

journal of nuclear materials

www.elsevier.com/locate/jnucmat

Low-temperature irradiation behavior of uranium–molybdenum alloy dispersion fuel ☆

M.K. Meyer [a,*], G.L. Hofman [b], S.L. Hayes [a], C.R. Clark [a], T.C. Wiencek [b], J.L. Snelgrove [b], R.V. Strain [b], K.-H. Kim [c]

[a] *Argonne National Laboratory, P.O. Box 2528, Idaho Falls, ID 83403, USA*
[b] *Argonne National Laboratory, 1700 S. Cass Avenue, Argonne, IL 60439, USA*
[c] *Korea Atomic Energy Research Institute, 150 Dukjin-Dong, Yusong-ku, Taejon 305-600, South Korea*

Received 15 November 2001; accepted 1 April 2002

Abstract

Irradiation tests have been conducted to evaluate the performance of a series of high-density uranium–molybdenum (U–Mo) alloy, aluminum matrix dispersion fuels. Fuel plates incorporating alloys with molybdenum content in the range of 4–10 wt% were tested. Two irradiation test vehicles were used to irradiate low-enrichment fuels to approximately 40 and 70 at.% ^{235}U burnup in the Advanced Test Reactor at fuel temperatures of approximately 65 °C. The fuel particles used to fabricate dispersion specimens for most of the test were produced by generating filings from a cast rod. In general, fuels with molybdenum contents of 6 wt% or more showed stable in-reactor fission gas behavior, exhibiting a distribution of small, stable gas bubbles. Fuel particle swelling was moderate and decreased with increasing alloy content. Fuel particles with a molybdenum content of 4 wt% performed poorly, exhibiting extensive fuel–matrix interaction and the growth of relatively large fission gas bubbles. Fuel particles with 4 or 6 wt% molybdenum reacted more rapidly with the aluminum matrix than those with higher-alloy content. Fuel particles produced by an atomization process were also included in the test to determine the effect of fuel particle morphology and microstructure on fuel performance for the U–10Mo composition. Both of the U–10Mo fuel particle types exhibited good irradiation performance, but showed visible differences in fission gas bubble nucleation and growth behavior.

1. Introduction

Since the 1980s, US policy [1] has encouraged the use of low enriched uranium (LEU, ^{235}U < 20 at.%) in fuels for all new research reactor designs worldwide and for conversion of existing reactors from higher enrichments. Due to the decrease in ^{235}U enrichment on conversion to LEU, the total density of uranium atoms in the fuel must be increased accordingly [2].

The simplest route for reactor conversion from higher enrichment to LEU fuel is to use standard fabrication technology and fuel geometry, that is by using one of the two common commercial fabrication processes to make LEU fuel in the same external configuration as higher enrichment fuel. The roll bonding process, used to make plate-type fuel, has been shown to be suitable for producing dispersions with fuel particle volume loading up to approximately 55 vol.% [3]. The other method, extrusion, used to make rod-type and tube-type fuels, is likely have a lower maximum fuel particle volume limit than roll bonding [4]. Thus in order to meet fissile atom density requirements at a fuel particle volume fraction of

☆ Work supported by the US Department of Energy Office of Non-proliferation and National Security under contract no. W-31-109-ENG-38.

* Corresponding author. Tel.: +1-208 533 7461; fax: +1-208 533 7863.
E-mail address: mitchell.meyer@anl.gov (M.K. Meyer).

0022-3115/02/$ - see front matter
PII: S0022-3115(02)00850-4

55% or less, fuel for high power test reactors requires fuel particles with uranium densities of greater than 15 000 kg U/m^3. There are two types of fuel that approach or meet this density criterion; metallic uranium alloys and the U_6Me family of intermetallics, where Me = Fe, Mn, Ni, or Ge.

The irradiation behavior of U_6Me plate-type dispersion fuel has been previously investigated as a candidate high-density fuel. U_6Fe and U_6Mn have been shown to have poor irradiation behavior in a dispersed thin plate configuration due to breakaway swelling of the fuel phase at relatively low burnup [5–7]. It is likely that other U_6Me compounds will behave in a similar manner. Metallic uranium alloys are then, by default, the only materials with the potential for use as the fuel phase in high-density LEU dispersion fuels for high power research reactors. It has been shown that γ-stable (cubic crystal structure) metallic fuels are more resistant to swelling than α-uranium-based (orthorhombic crystal structure) fuels under low-burnup, high-temperature irradiation conditions. γ-U is not thermodynamically stable under the fabrication and irradiation conditions of interest, however some alloys of uranium can remain in the γ-phase in a metastable state indefinitely at room temperature, and for long periods of time at elevated temperature. Of particular interest are U–Mo and U–Nb–Zr alloys. Beghi [8] provides a summary of physical properties and irradiation data known for U–10Mo alloys prior to 1967; phase stability information on U–Nb–Zr alloys can be found in [9–13].

Aluminum-clad dispersion fuels in some reactors routinely attain 80% peak ^{235}U burnup. Peak fuel temperature in these applications is generally less than 523 K. No fuel data were available for metallic alloy fuels under these high-burnup, low-temperature conditions. A scoping irradiation test was thus designed to investigate the performance of a series of enriched uranium alloys dispersed in aluminum to high burnup at $T \leqslant 373$ K. A test matrix containing U–10Mo, U–8Mo, U–6Mo, U–4Mo, U–6Mo–lPt, U–6Mo–0.6Ru, U–10Mo–0.05Sn, U–9Nb–4Zr, U–6Nb–4Zr, U–5Nb–3Zr (values in wt%) provided a broad range of potential fuel candidates. U_3Si_2 fuel specimens were included to provide a standard for comparison to a commercial fuel with known performance. This paper reports details of the irradiation test and post-irradiation examination (PIE) results from testing of binary U–Mo alloy compositions ranging from 4 to 10 wt% molybdenum. Results from irradiation testing and PIE of the U–Nb–Zr alloys are presented elsewhere [14].

2. Fuel test specimen fabrication and characterization

2.1. Preparation of fuel materials

Two types of U–Mo fuel powder were used in these experiments. The majority of the fuel material was powder of irregular morphology made by collecting filings from U–Mo alloy rods. Alloys were melted in an induction furnace and cast into rod form. The alloys were wrapped in tantalum foil and encapsulated in evacuated stainless steel tubes prior to a homogenization heat treatment at 1173 K for 288–360 ks (80–100 h). Powder was produced by grinding the alloy rods with a tungsten carbide (WC) rotary file; the metal fuel filings produced were sieved to −50 mesh ($d < 300 \times 10^{-6}$ m). Some WC contamination was introduced into the fuel powder due to tool wear, [15] as detected by metallography, tool mass loss, and X-ray diffraction (XRD).

The second type of alloy powder was made by a spinning disk melt atomization process with the nominal composition of U–10Mo. Details of the atomization process are given elsewhere [16]. Chemical analysis of fuel alloy rods and of atomized powder is given in Table 1.

2.2. Fabrication of fuel test specimens

The fuel powder described in Section 3.1 was used to make fuel plates using the basic fabrication procedure described in detail in Ref. [17], although the fuel test coupons used in these experiments are somewhat smaller. The dimensions of the fuel plates fabricated for irradiation were 7.62×10^{-2} m $\times$ 2.22×10^{-2} m ($L \times W$), and 1.27×10^{-3} m in thickness. The plate assemblies

Table 1
Chemical analysis of U–Mo fuel materials

Material	Total U (±0.5 wt%)[a]	^{235}U (±0.5 wt%)[a]	Mo (±10 wt%)[a]	C (±25 wt%)[a]	O (±25 wt%)[a]
U–10Mo[b]	89.5	19.5	10.3	0.013	0.007
U–10Mo atomized powder	89.4	19.8	10.3	0.032	–
U–8Mo[b]	91.4	19.5	8.1	0.010	0.016
U–6Mo[b]	93.5	19.1	6.1	0.014	0.010
U–4Mo[b]	95.9	19.5	4.0	0.053	0.008

[a] Relative error at 2σ.
[b] Chemical analysis of fuel pin casting from which powder was produced.

were hot rolled at 773 K, using six rolling passes to reduce the total thickness of the plates from 6.7×10^{-3} to 1.4×10^{-3} m. Cylindrical fuel meat compacts were used, resulting in an elliptical fuel zone after fabrication, with a minor diameter of 9.5×10^{-3} m and a major diameter of $\sim 4.8 \times 10^{-2}$ m. Hot rolling was followed by a blister anneal at 758 K for 3.6 ks. Total time above 750 K was 6.3 ks. Final reduction to 1.27×10^{-3} m thickness was accomplished by cold rolling. The resulting fuel test coupons consist of a fuel zone of 4.2×10^{-4} m thickness clad by 4.2×10^{-4} m thick aluminum. The fuel matrix is nominally pure aluminum; the cladding is commercial 6061 aluminum alloy.

X-ray radiography was used to image the fuel zones within each specimen. The X-ray film density of the fuel plates was measured and compared to that of a set of uranium alloy standards with known thickness and composition. Using the average fuel meat thickness value of 4.2×10^{-4} m, fuel volume loading was calculated from film density. These data are given in Table 2, along with data on irradiation test conditions.

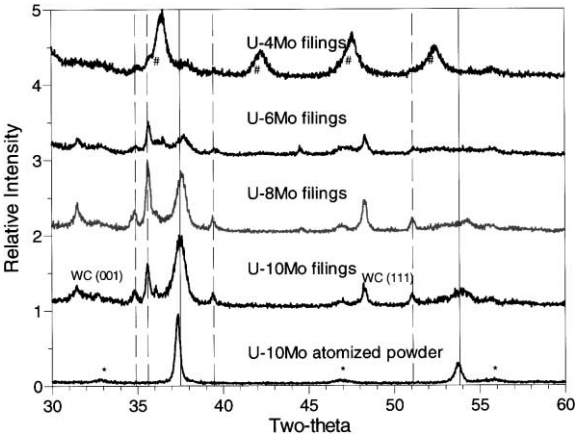

Fig. 1. XRD patterns of fuel particles after fuel plate fabrication and separation of fuel phase from aluminum matrix. Solid vertical lines denote γ-U peaks, dashed lines denote α-U, and ∗ denotes UO_2 diffraction peaks. Location of major WC peaks are marked. U–4Mo pattern shows predominantly a cubic phase similar to UAl_3, denoted by #.

2.3. Pre-irradiation characterization of fuel specimens

2.3.1. X-ray diffraction

Prior to fuel plate fabrication, XRD patterns indicated that all fuel alloy particles were nominally in the cubic γ-(U,Mo) solid solution phase [18]. Previous investigations implicate stress as a cause of phase changes in 'stabilized' uranium alloys [19]. This possibility and the shallow penetration depth of Cu K X-rays in uranium metal may mask the presence of other phases. Patterns recorded from U–4Mo and U–6Mo were very diffuse due to extensive plastic deformation introduced on filing.

After fuel plate fabrication, fuel powder was recovered from the aluminum-clad plates by dissolution of the aluminum in a 6 M aqueous sodium hydroxide solution at 373 K. XRD patterns were taken from these fuel particles to determine their pre-irradiation crystal structure; these are shown in Fig. 1. After fabrication and annealing at $T > 750$ K, a significant amount of orthorhombic α-U is detected in addition to γ-U in U–10Mo and U–8Mo filings. The presence of α-U was established by the presence of the (1 1 0), (0 2 1), (0 0 2), (1 1 1), and (1 1 2) reflections. The peak intensity of α-uranium was found to increase with decreasing uranium content, consistent with metallographic observations. This behavior is predicted by published transformation diagrams [20–24]. Diffraction peaks due to WC, UO, and UO_2 were also present in the U–10Mo,

Table 2
Fission density and burnup of irradiated U–10Mo fuel test coupons

Composition (wt%) nominal	Plate no.	Avg. uranium density[a] (10^3 kgU m^{-3})	^{235}U burnup[b] (avg. %)	Core fission density (10^{27} m^{-3})	Fuel particle fission density (10^{27} m^{-3})	Avg. fuel fission rate (10^{20} m^{-3} s^{-1})
U–10Mo	A003	4.9	40	0.8	2.7	3.3
U–10Mo	A005	4.5	69	1.4	4.9	2.4
U–10Mo^{atom}	V002	4.4	39	0.9	2.7	3.3
U–10Mo^{atom}	V003	4.3	70	1.4	5.0	2.5
U–8Mo	B002	4.6	43	0.9	3.1	3.8
U–8Mo	B004	4.4	70	1.4	5.2	2.6
U–6Mo	C004	4.9	43	1.0	3.2	3.9
U–6Mo	C003	4.6	67	1.4	5.2	2.6
U–4Mo	D002	4.7	42	0.8	3.3	4.1
U–4Mo	D005	4.6	69	1.5	5.6	2.8

[a] Density calculated from X-ray absorption measurements.
[b] Burnup calculated from ATR core model.

U–8Mo, and U–6Mo patterns. UO is a non-equilibrium phase that forms as a surface film. WC was introduced during powder production (see Section 2.1). In contrast to the heavily cold worked fuel particles, well formed WC crystals produce a more intense peak, thus WC contamination was present in amounts less than inferred from peak height ratios. Due to the diffuse pattern and interfering diffraction peaks from impurity phases, the presence of γ-U in U–6Mo could not be definitively established. The primary phase detected in U–4Mo fuel was UAl_3, consistent with SEM examination showing a shell of fuel–matrix interaction product surrounding fuel particles. α-U is also detected by XRD in U–4Mo; indications of γ-U were not present.

The post-fabrication U–10Mo atomized powder pattern showed that only the metastable γ-phase and a small amount of UO_2 that formed during fabrication or preparation of specimens for diffraction were present. The atomized powder had approximately the same thermal history as the fuel filings, suggesting that extensive plastic deformation contributes to accelerated decomposition of the γ-phase in the U–10Mo filings.

2.3.2. Metallographic examination

Fig. 2(a) shows a low-magnification secondary electron (SE) image of the 'meat' region of a fuel specimen containing U–10Mo filings. The irregular shape of the fuel particles is evident. There is no visible fuel/aluminum interaction after the elevated temperature fabrication process described above.

An SE image of U–10Mo fuel particles after etching in a 1:1 solution of nitric and phosphoric acid is shown in Fig. 2(b). This image shows that there are two distinct microstructural regions in the fuel. A higher-magnification image of the interface between these regions is shown in Fig. 2(c); the region on the left is the phase that appears in dark contrast in Fig. 2(b). This region has a topologically rough appearance, and is likely associated with decomposition of the metastable gamma phase. Energy dispersive chemical analysis (EDS) gave the same bulk composition for both regions of the sample. The microstructural scale of the rough region is on the order of 1×10^{-7} m, smaller than the diameter of interaction of the electron beam with the sample, thus no determination of compositional difference within the fine structure could be made. The featureless areas of the sample with brighter contrast are inferred by microstructure [25] and XRD data to be single phase γ-(U,Mo).

The lower-alloy fuels tended to be more easily converted to powder and showed less WC contamination. As the alloy content decreased, the area fraction of the topographically rough microstructure associated with γ-U decomposition phases increased. This observation is consistent with the relative α/γ intensity ratios in the XRD patterns, which show that the quantity of post-fabrication α-U increases as alloy content decreases (Fig. 1). A heavily etched SE image of U–8Mo is shown in Fig. 3(a). As was the case for the U–10Mo alloy fuels, there is little fuel–matrix interaction.

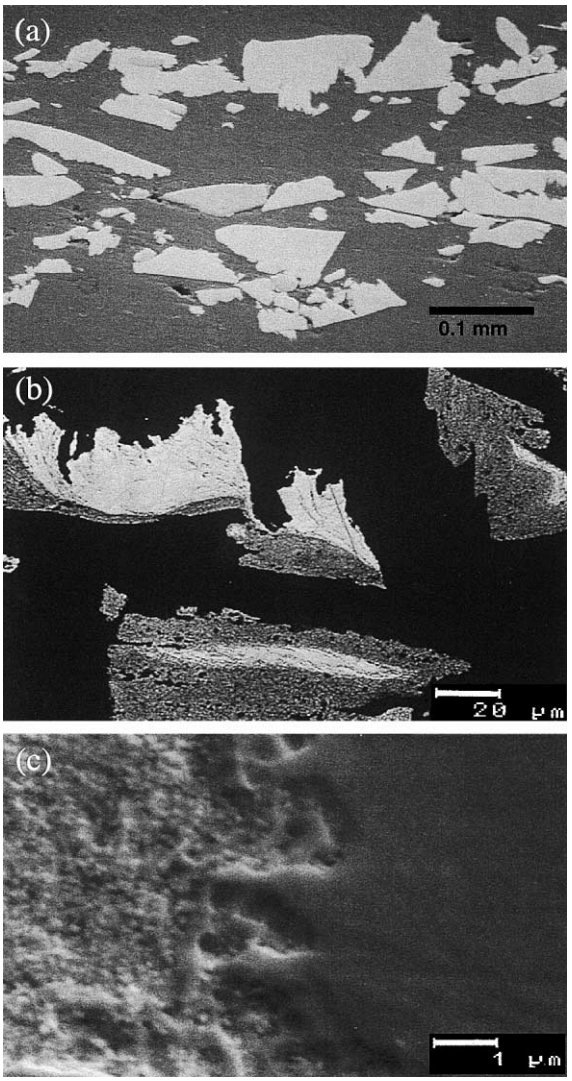

Fig. 2. Polished cross-section of uranium-10 wt% molybdenum filings in aluminum matrix, prior to irradiation. SE images: (a) unetched, showing little reaction between fuel particles and matrix on fabrication; (b) etched, showing two distinct microstructural regions within the fuel particles; (c) interface between 'smooth' and textured regions of fuel particle microstructure.

It appears that there is a critical molybdenum level between 6 and 8 wt% below which the out-of-pile thermal reaction of U–Mo alloys with aluminum occurs at an accelerated rate during fuel plate fabrication. A backscattered electron (BSE) image of U–6Mo fuel is shown in Fig. 3(b). The light areas in the micrograph are unreacted fuel, the black areas are the aluminum matrix.

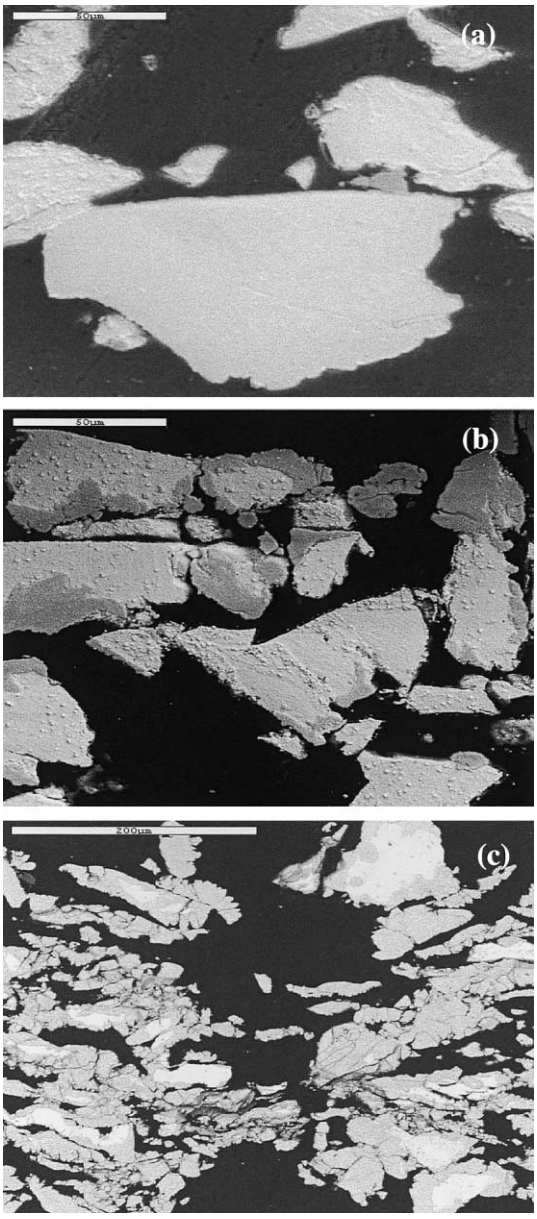

Fig. 3. U–8Mo, U–6Mo, and U–4Mo fuel microstructures prior to irradiation. (a) SE image of etched U–8Mo showing minimal fuel/matrix interaction on fabrication and striations due to etching of dual microstructure; (b) U–6Mo (etched) showing significant fuel/matrix interaction and absence of γ-U; (c) U–4Mo, showing almost complete fuel/matrix interaction consistent with XRD results (Fig. 1).

The gray regions were identified by EDS as $(U,Mo)Al_3$. The reaction of the fuel particles with the aluminum matrix did not proceed along a uniform front. As the fuel particle alloy content is decreased from 6 to 4 wt%, the rate of fuel/aluminum interaction shows further increase. A post-fabrication image of U–4Mo fuel is shown in Fig. 3(c). Atomic number contrast was used to estimate the fraction of unreacted alloy in these fuels. Analysis of BSE images indicates that 56% of the original fuel remains unreacted in the U–6Mo dispersion; 22% remains unreacted after fabrication of U–4Mo specimens.

The U–4Mo fuel zone contained a significant fraction of porosity not present in the other fuels. Fuel plates produced by hot deformation methods using brittle oxide or intermetallic compounds at high volume fractions contain a significant fraction of porosity due to fracturing of fuel particles [26]. It is likely that formation of a large amount of brittle aluminide phase caused a similar situation in the U–4Mo fuel plates.

A micrograph of an atomized fuel particle etched in a solution of nitric acid, acetic acid, and water (1:1:2) is shown in Fig. 4(a). There is no visible fuel/aluminum interaction. A higher-magnification image (Fig. 4(b)) shows the microstructure that results from the atomization process. Visible in the micrograph are primary grain boundaries due to solidification fronts, and a cored/cellular microstructure within each primary grain. The interior of each cell is molybdenum rich relative to the cell boundary. Consistent with XRD, no decomposition phases were observed by SEM. The particles are composed primarily of a γ-(U,Mo) solid solution with compositional variations due to 'coring' during solidification. Further microstructural details are given in Refs. [27,28].

3. Irradiation testing

3.1. Irradiation test conditions

Irradiation testing was carried out in two irradiation vehicles (RERTR-1 and RERTR-2) in small I-hole positions located in the reflector region radially outside of the Advanced Test Reactor (ATR) core [29]. The I-positions are vertical holes, 3.8×10^{-2} m in diameter. These positions receive a relatively high thermal neutron flux; average fission rates are given in Table 2. The irradiation vehicles consisted of a flow-through 'basket' holding eight vertically stacked, flow-through capsules. The capsules resemble miniature test reactor fuel elements. Each capsule held four fuel specimens in a configuration such that the long dimension of the microplates is parallel to the reactor primary coolant flow. Flow-through spacers at the top and bottom of the stack of capsules were used to center the experiment about the core axial mid-plane.

The first experiment, RERTR-1, was discharged from the ATR after 94 effective full-power days (EFPDs) of irradiation at calculated average burnups between 39 and 45 at.% ^{235}U. RERTR-2 was discharged

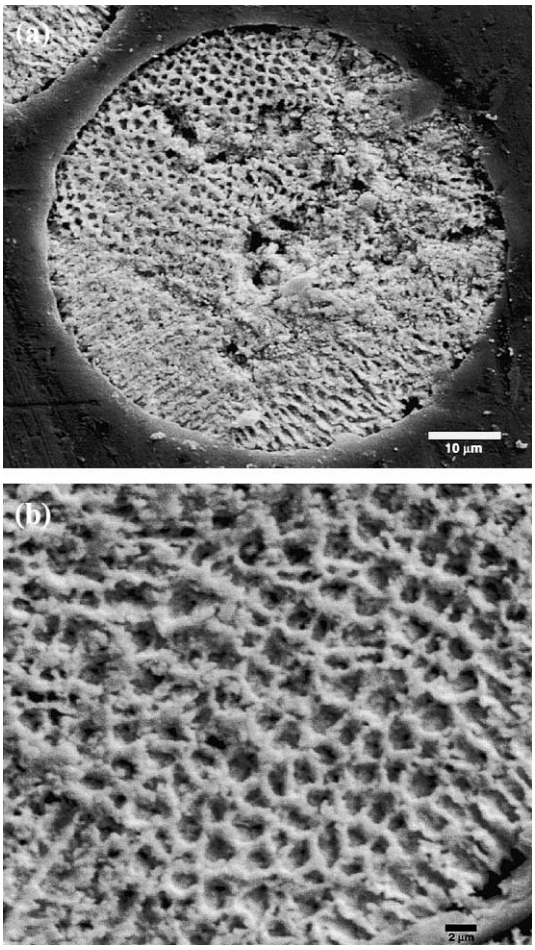

Fig. 4. U–10 wt% Mo atomized fuel powder, prior to irradiation. Etched SE images: (a) Primary grain boundaries are marked by changes in cell orientation. No detectable fuel/matrix interaction; (b) cellular structure that results from rapid solidification during atomization.

following 232 EFPDs at calculated burnups between 65 and 71 at.%. The fuel centerline temperature of these plates during irradiation was calculated to be approximately 65 °C in both experiments. Fission density and burnup are listed in Table 2 for specimens discussed here. The core fission density refers to the fission density averaged over the entire fuel/aluminum matrix volume in the fuel plate; the fuel particle fission density refers to the fission density in the fuel particles themselves. Note that the fuel particle fission densities are relative to the as-fabricated fuel meat uranium density; hence they do not account for fuel particle volume increase owing to fuel–matrix interaction.

3.2. Burnup analysis

Burnup analysis was performed by measuring the relative abundance of uranium isotopes prior to and after irradiation using mass spectrometry. The pre-/post-irradiation ^{235}U isotopic ratios corrected for uranium atom density were used to calculate burnup. Burnup samples were taken from specimens irradiated in the top, center, and bottom core regions of the experiments. Measured values were used to verify calculations made using an ATR-specific MCNP model. Due to the small size of the fuel test coupons, all of the fuel in a particular coupon was required for burnup analysis, and no direct measurement of burnup was available for portions of plates subject to destructive examination. Calculated and measured values for five specimens are given in Table 3. Burnup calculations overestimated the actual measured burnup in the two plates located in the capsules farthest above the axial mid-plane by 3.8% and 4.5%. Specimens located near and below the core axial mid-plane had measured burnup values within 2% of calculated values. Post-irradiation analysis results reported in this paper are for specimens irradiated in positions below the core centerline.

4. Post-irradiation examination

4.1. Non-destructive examination

Visual inspection of the fuel specimens from both RERTR-1 and RERTR-2 was performed. Significant corrosion of the microplate surfaces was noted, being

Table 3
Burnup values for fuel plates from RERTR-1 and RERTR-2

Plate	Composition	Experiment	Distance from mid-plane (m)	Calculated burnup (%)	Measured burnup (%)
F001	U–6Nb–4Zr	RERTR-1	0.31	40	36.2
F003	U–6Nb–4Zr	RERTR-2	0.31	66	61.5
J003	U–9Nb–3Zr	RERTR-2	0.04	71	73.0
J001	U–9Nb–3Zr	RERTR-1	0.04	45	46.3
D004	U–4Mo	RERTR-1	−0.31[a]	39	39.0

[a] Negative value indicates plate location below core axial mid-plane.

more severe over the fuel zone. Pitting corrosion was observed on the surface of five specimens. These features were not related to fuel performance; no unusual features were observed on metallographic examination of the fuel zone cross-section at the pit location. Cladding erosion problems are common to aluminum fuel in the ATR that has not been pre-treated to form a coherent oxide layer prior to reactor insertion [30].

Plate thickness measurements were made on a grid containing seven locations inside the fuel zone. One measurement was taken outside the fuel zone for reference. For fuel plates in the low-burnup RERTR-1 test, the averages of the seven thickness measurements within the fuel zone was smaller than the as-fabricated plate thickness, indicating that either the fuel experienced a meat volume decrease or erosion of the cladding occurred during irradiation. High-burnup fuel plates (RERTR-2) showed thickness increases of less than 1×10^{-4} m. Metallographic examination revealed a rough cladding surface with no adherent scale layer present, confirming the erosion or spallation of a corrosion product.

Axial gross and isotopic gamma ray spectroscopy was performed on 27 specimens from RERTR-1 and 32 specimens from RERTR-2. The Nb-95 axial traces through the fuel zones, when normalized with respect to the axial uranium density (which varies due to the elliptical shape of the fuel zone), are essentially flat. This indicates that the burnup is uniform within each specimen, which was expected due to their small size.

4.2. Post-irradiation metallographic examination

Optical micrographs of the five alloy fuel types at approximately 40% and 70% burnup are shown in Figs. 5 and 6, respectively. An overview of the differences in behavior as a function of alloy content and microstructure can be gained by direct comparison. The microstructure of U_3Si_2 fuel irradiated in this experiment as a control is also shown in Fig. 6(f). The U_3Si_2 fuel particles were made by mechanical particle size reduction and are of the type currently used in many research reactors. Specimens incorporating fuel particles with more than 6 wt% molybdenum show no gross fuel swelling or indication of fuel growth or void formation by tearing. (Here fuel growth is taken to mean anisotropic shape change.) Fission gas bubble volume is seen to increase as the molybdenum content of the alloy decreases. The population and volume fraction of fission gas bubbles in the U_3Si_2 particles is intermediate to that of U–6Mo and U–8Mo. The U–6Mo alloy forms a thicker fuel/matrix interaction layer during irradiation than the U–8Mo and U–10Mo alloys. The fuel/aluminum reaction layer does not generally exhibit visible fission gas bubbles, although there are a few isolated occurrences. The behavior of the U–4Mo specimen differs markedly from the higher-alloy fuels. Considerable fuel/aluminum reaction occurred at high burnup, visible as a layer of uniform thickness and slightly different contrast compared to the reaction product that formed out-of-pile (see Fig. 10). Large fission gas bubbles are present in the unreacted portions of the fuel alloy.

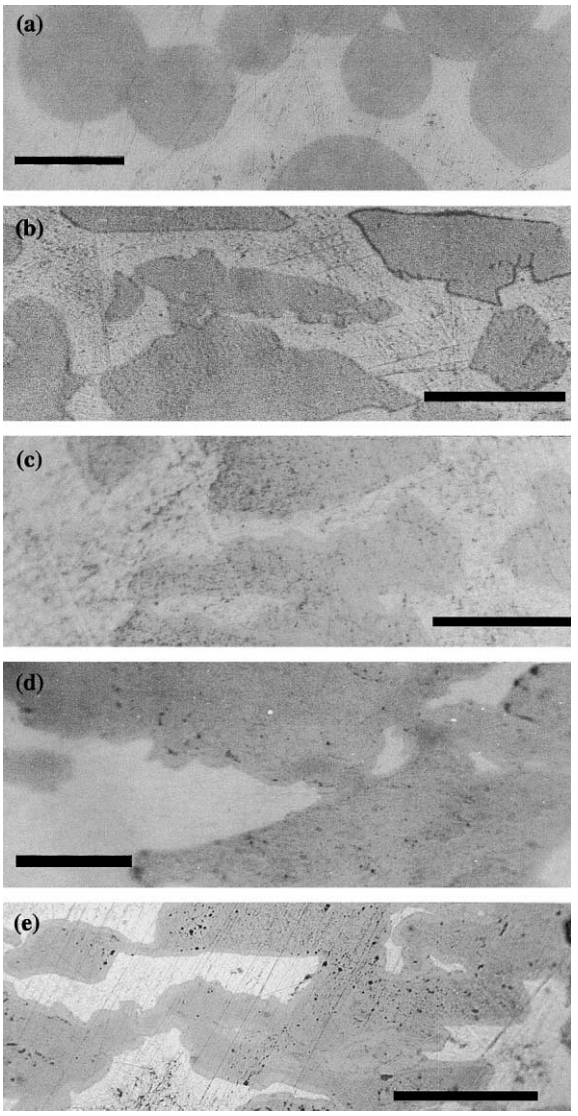

Fig. 5. Comparison of U–xMo fuel particles at approximately 40 at.% ^{235}U burnup. Optical micrographs of (a) U–10Mo atomized powder, (b) U–10Mo filings, (c) U–8Mo filings, (d) U–6Mo filings, (e) U–4Mo filings. Scale bars represent 50 μm.

Shown in Fig. 7(a) is a low-magnification SE image of a fracture surface from a U–10Mo filing after irradiation to a fission density of 2.7×10^{27} m^{-3}. This fuel shows a microstructure that varies from particle to particle and within individual particles, consistent with the non-uniform microstructures of the as-fabricated

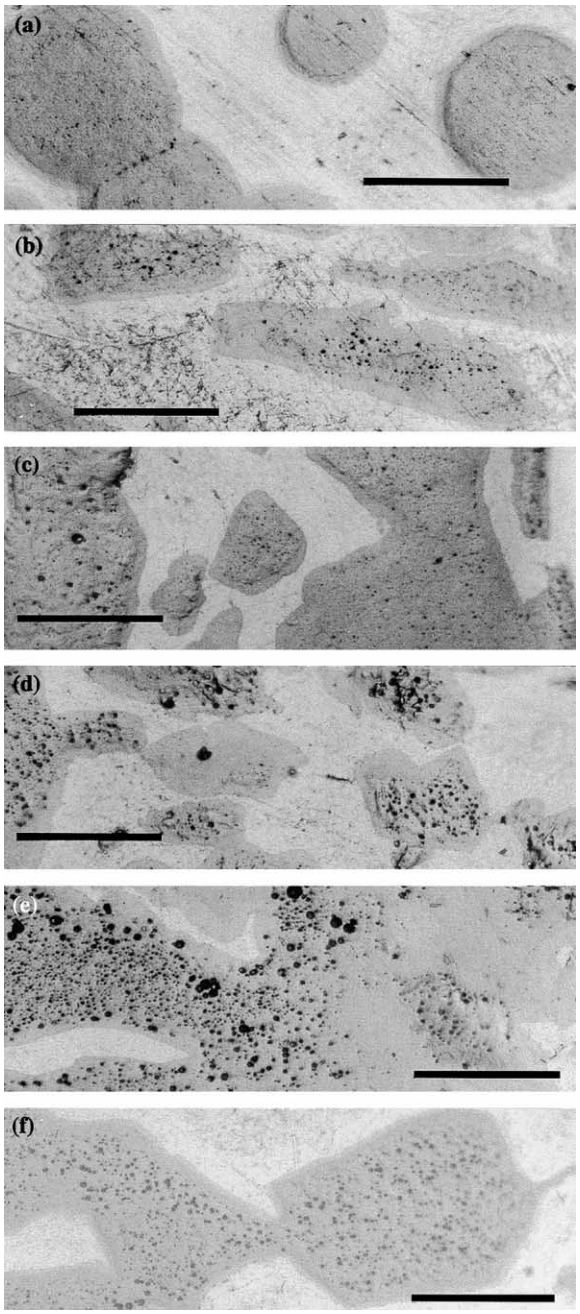

Fig. 6. Comparison of U–*x*Mo fuel particles at approximately 70 at.% ^{235}U burnup. Optical micrographs: (a) U–10Mo atomized powder, (b) U–10Mo filings, (c) U–8Mo filings, (d) U–6Mo filings, (e) U–4Mo filings, and (f) U_3Si_2 powder. Scale bars represent 50 μm.

fuel particles shown in Fig. 1. Some areas of the fuel have a stepped fracture surface, with low bubble density and groups of bubbles appearing at the edges of the fracture steps. The fracture has a 'granular' appearance at the step edges where bubbles are present. A polished and etched SEM specimen, shown in Fig. 7(b), shows the distribution of fission gas bubbles and bubble-free areas in these low-bubble-density regions. Gas bubbles appear to be arrayed on the boundaries of small grains with a size range of $1–4 \times 10^{-6}$ m. These 'stepped' fracture regions, by analogy with the microstructure of the γ-phase atomized fuel particles, likely correspond to the single phase γ-(U,Mo) regions seen in the pre-irradiation microstructure. The second type of fracture morphology shows a higher density of bubbles (Fig. 7(a), left) distributed throughout the fuel. This type of region is likely associated with the decomposition microstructure identified as the dark contrast regions in Fig. 2. No quantification of the relative areas of each type of post-irradiation fracture morphology could be made on the basis of fractographs.

Fig. 7(c) and (d) show the development of the fracture and fission gas bubble morphology of U–10Mo on irradiation to a higher fission density (4.9×10^{27} m^{-3}, 69% burnup). The dual fracture morphology is retained at this higher fission density. The granular fracture regions shown in Fig. 7(c) give the appearance of a faceted surface, with bubbles at the intersections of the facets. The stepped fracture surface seen at low burnup is no longer present, and has likely evolved into the fine-grained microstructure shown in Fig. 7(c). Fig. 7(d) shows an area with a planar fracture surface and a bimodal bubble distribution, similar to that seen at low burnup (Fig. 7(a), left).

SE fractographs of U–8Mo filings after irradiation to 3.1×10^{27} fissions m^{-3} are shown in Fig. 8(a) and (b). Comparison of this fuel with U–10Mo filings (Fig. 7) shows an increased fission gas bubble population in the U–8Mo alloy relative to U–10Mo at approximately the same burnup. The granular type fracture produced in regions with a large population of small gas bubbles seen in U–10Mo at high burnup has developed in this alloy at lower burnup. The microstructural evolution of U–8Mo at higher burnup is shown after 5.2×10^{27} fissions m^{-3} in Fig. 8(c) and (d). There does not appear to be a strong dependence of interaction layer growth rate on composition in the range of 8–10 wt% molybdenum; the interaction layer thickness is approximately the same as that found on U–10Mo.

Comparison of a U–6Mo fracture surface at low burnup in Fig. 9(a) (fission density of 3.2×10^{27} m^{-3}) to the U–10Mo particle fracture surface at higher burnup (Fig. 7(c) 4.9×10^{27} m^{-3}) reveals a close resemblance. U–6Mo fuel is shown at 5.2×10^{27} fissions m^{-3} in Fig. 9(b) and (c). The fission gas bubble population and size are larger at high burnup for U–6Mo than for U–8Mo and U–10Mo alloys; gas bubble range in size up to 2×10^{-6} m. Comparison of the microstructures as a function of composition suggests that the same type of fission and fission gas induced microstructural changes

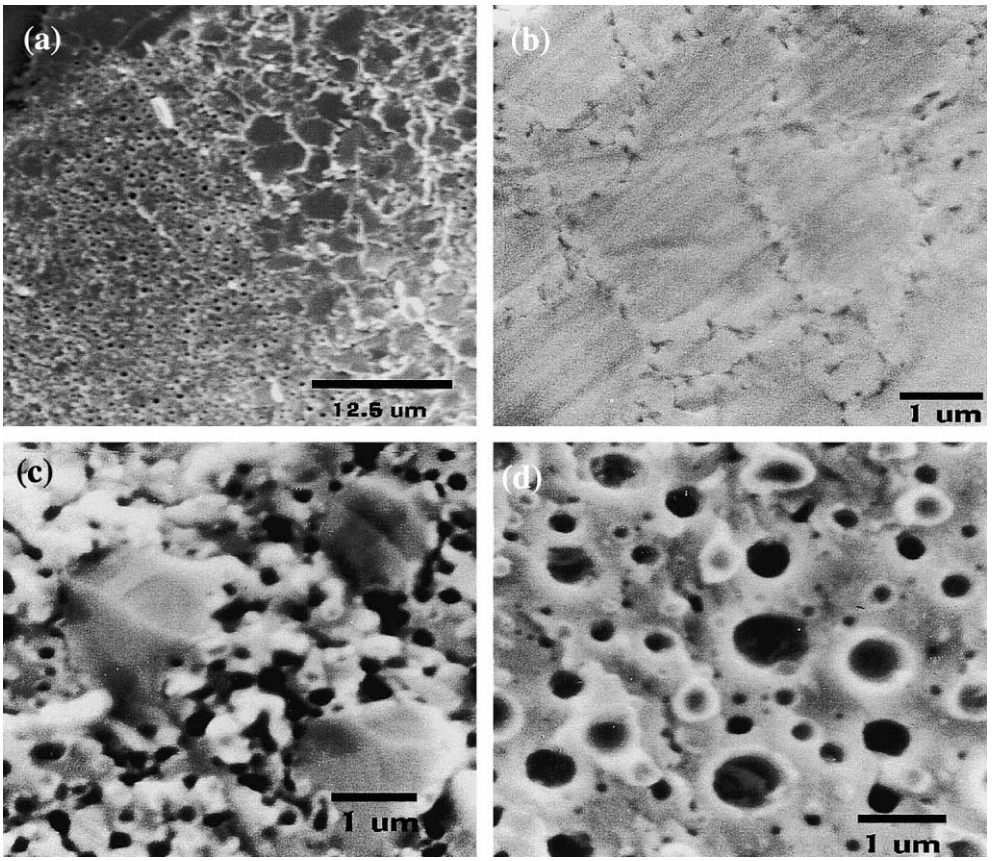

Fig. 7. SE Images of U–10Mo fuel particles produced by filing: (a)–(c) are specimen A003 at 2.7×10^{27} fissions m^{-3}. (a) Image showing two distinct regions of fracture morphology and fission gas bubble population. Region to lower left shows high bubble density and granular fracture; upper right shows low bubble population and stepped fracture surface. (b) Polished and etched microstructure of low-bubble-density area, (c) and (d) are from specimen A005 at 4.9×10^{27} fissions m^{-3}. (c) Fracture surface showing granular morphology and micrometer scale regions where bubbles have not developed. (d) Planar fracture surface showing population of larger fission gas bubbles.

are occurring in all fuels in the composition range from 6 to 10 wt% molybdenum, but at a faster rate in the lower-alloy fuels.

There occurs a definite change in fuel behavior on reducing the alloy content from 6 to 4 wt% molybdenum. Most of the fuel alloy has reacted with the aluminum matrix during fabrication and irradiation. The aluminide phase that forms appears to behave well under irradiation (Fig. 10(a)). Fuel particles have grown and linked together as a result of gas-driven swelling and fuel–matrix interaction; in some regions of the fuel, a continuous network of fuel particles has been formed. Fuel that has not reacted with the matrix and remains metallic has a high density of large fission gas bubbles. It is evident from the appearance of some gas bubbles (Fig. 10(a)) that growth by linking of small bubbles to form larger bubbles has occurred. An SE image of the fracture surface of the fuel in Fig. 10(b) shows regions of high densities of small gas bubbles adjacent to regions with a lower density of larger gas bubbles. Fission gas bubbles have grown in size to 6×10^{-6} m in diameter.

SE images taken from U–10Mo atomized fuel powder at a fission density of 2.7×10^{27} m^{-3} are shown in Fig. 11. In general, the microstructural features observed in this fuel were found to be uniform from particle to particle. A low-magnification image showing fuel particles, matrix, and interaction layer is shown in Fig. 11(a). The surface morphology of the aluminide interaction layer can be seen on the small particle to the right in the micrograph. Fig. 11(b) shows that gas bubbles are small and distributed primarily as linear features. Fracture surfaces are composed of flat steps with changes in fracture elevation coincident with lines of bubbles. The fracture surface gives the appearance that fission gas bubbles have nucleated and grown mainly on primary grain boundaries. This behavior is consistent with the

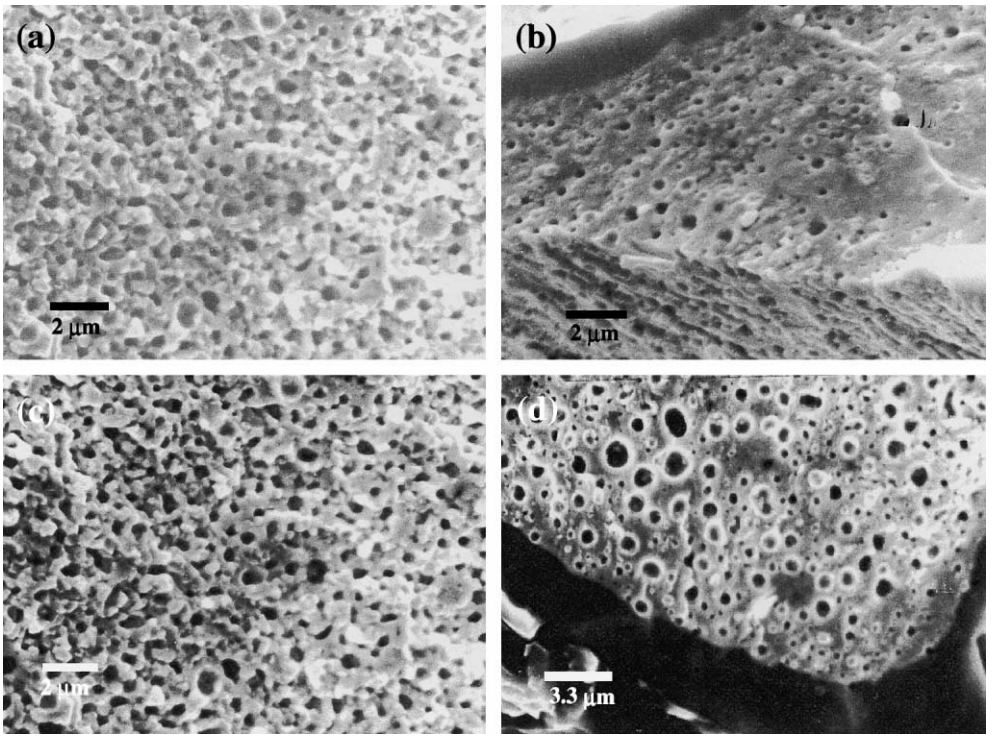

Fig. 8. U–8Mo filings. (a) and (b) show fracture surfaces of specimen B002 irradiated to a fission density of 3.0×10^{27} m^{-3}. (c) and (d) are fracture surfaces of specimen B004 at a fission density of 5.2×10^{27} m^{-3}. Note granular fracture morphology in (a) and (c) vs. planar fracture in (b) and (d).

general observation that grain boundaries are the preferred site for fission gas bubble nucleation and growth [31], particularly at lower irradiation temperatures. There are also a lesser number of bubbles that have nucleated within the primary grains. A polished and etched surface is shown in Fig. 11(c). The observed contrast is consistent with the cored structure of the as-atomized fuel powder; the dark areas are the molybdenum-enriched core, and the lighter-contrast regions are molybdenum depleted relative to the average sample composition. Fission gas bubbles are also seen to nucleate in association with the molybdenum depleted cell boundaries at this burnup.

Micrographs of U–10Mo atomized fuel after exposure to a fission density of 5.0×10^{27} m^{-3} are shown in Fig. 12. At this burnup level, gas bubbles no longer appear as linear features (Fig. 12(a)), neither are they uniformly distributed across the fractures surface. A higher-magnification SE image of a post-irradiation fracture surface is shown in Fig. 12(b). Fracture surfaces of areas with a high density of fission gas bubbles have a granular appearance, identical to fractures seen in fuel particles made by filing. Interspersed with these areas are locations with low bubble density. An SE image of a polished and etched specimen is shown in Fig. 12(c). The volume of the bubble-free areas has decreased significantly at higher burnup, but the microstructure maintains a cellular appearance. Contrast due to compositional variations (if present at this burnup) is obscured by the high density of gas bubbles and by solid fission product formation. Bubble-free areas are present, however, presumably in the molybdenum rich cell interior regions of the solidification microstructure (Fig. 12(d)).

Fission gas bubble volume is an indicator of gas-driven swelling. The volume of fission gas bubbles within the unreacted portions of fuel particles was estimated by using contrast-based image analysis on a combination of SEM and optical images. The area of bubbles larger than 1×10^{-6} m in diameter was determined using 500× optical images of as-polished specimens. SEM images of magnification 5000–10 000× allowed resolution of bubbles in the range of $0.1–1 \times 10^{-6}$ m. Polished SEM samples were etched for 3–5 min in an aqueous solution of 10% nitric acid and 10% hydrogen peroxide to reveal small bubbles that were obscured by 'smearing' during sample polishing. In the case of U–4Mo, measurements were taken only from the center of fuel particles that were judged not to have reacted with aluminum during fabrication. Gas bubble volume data for fuel

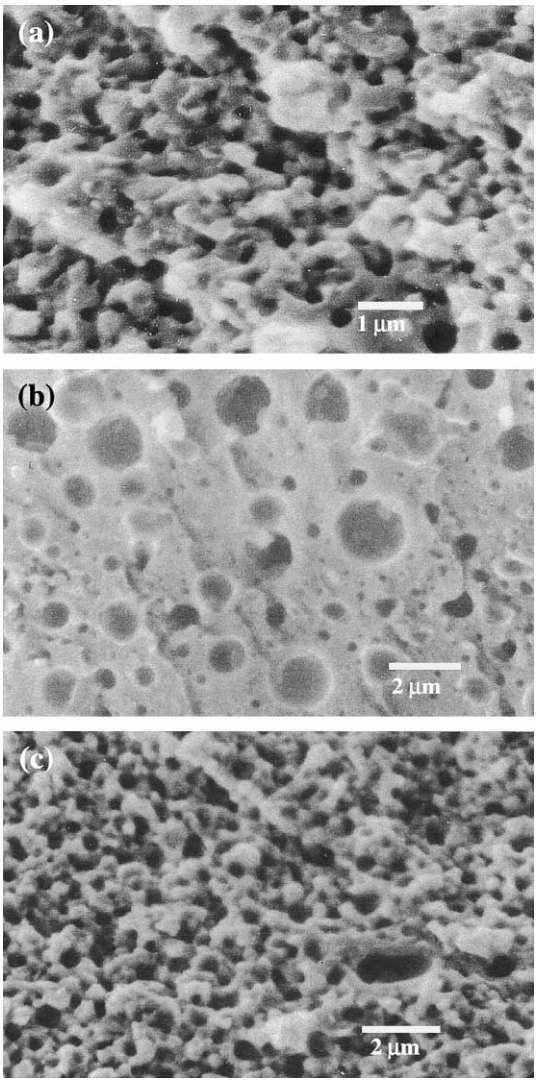

Fig. 9. U–6Mo alloy. (a) Fracture surface of specimen C004 after irradiation to 3.2×10^{27} fissions cm^{-3}. (b) Fracture surface of specimen C004 after irradiation to 5.2×10^{27} fissions cm^{-3} showing distribution of large fission gas bubbles. (c) Specimen C004 showing granular fracture and population of fine bubbles.

particles at approximately 70 at.% ^{235}U burnup is given in Table 4.

5. Discussion

Two general conclusions about the irradiation behavior of U–Mo alloy-based dispersion fuel can be drawn from the examination of these specimens. These are that (1) the pre-irradiation fuel particle microstructure and alloy content have a significant effect on the behavior of fission gas within the fuel alloy, and (2) the alloy content of the fuel particle has an effect on the rate of fuel/matrix interaction.

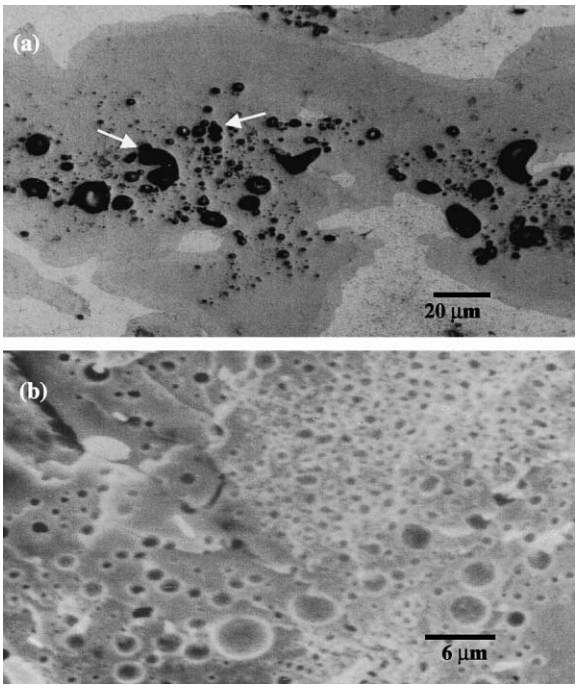

Fig. 10. U–4Mo fuel specimen D005 after irradiation to 5.6×10^{27} fissions cm^{-3}. (a) Optical micrograph showing large fission gas bubbles and evidence for interlinking (arrows), (b) SE image of fracture surface.

5.1. Effects of pre-irradiation fuel particle microstructure and alloy composition on fission gas behavior

Data in Table 4 indicate that measured fission gas bubble volume increases monotonically with decreasing molybdenum content in specimens produced from fuel filings. Previous work by Johnson and Holland [32] reported that swelling of U–Mo alloys increased in inverse proportion to molybdenum content for a variety of fission rates and temperatures from 753 to 973 K. Increased swelling rates in this regime have been associated with transformation from the γ-phase [33]. In the current set of specimens with differing alloy content produced by filing, however, the effect of alloy content and the resulting pre-irradiation phase array are intertwined with effects due to the high concentration of defects in the crystalline structure. The pre-irradiation microstructure is linked to both the process used to fabricate the fuel particles and the molybdenum content of the fuel particle alloys. The as-fabricated particle microstructure consists of regions of cold worked γ-phase alloy and regions where the alloy is in various stages of

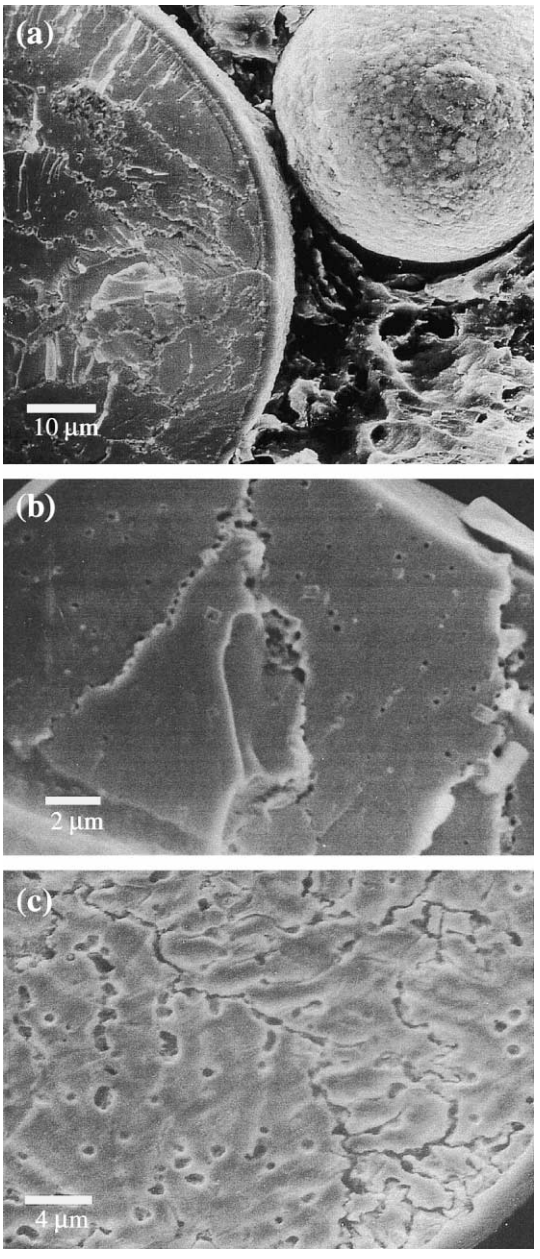

Fig. 11. SE images of U–10Mo atomized powder after irradiation to a fission density of 2.7×10^{27} m^{-3}. (a) Fracture surface showing interaction layer. (b) Fracture surface showing linear arrangement of fission gas bubbles. (c) Polished and etched surface showing relationship between local composition and growth of fission gas bubbles. Light regions are low-molybdenum content cell boundaries.

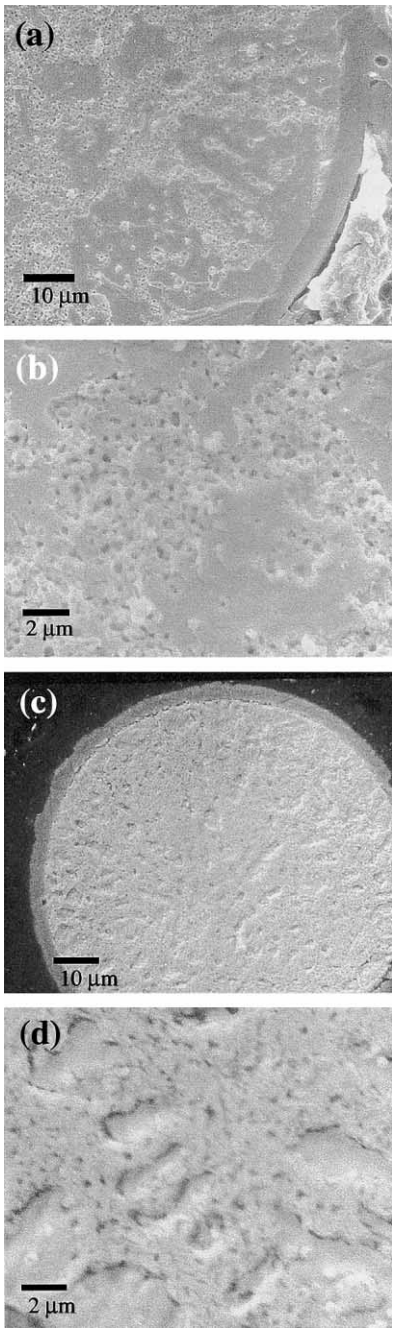

Fig. 12. SE images of U–10Mo atomized powder after irradiation to a fission density of 5.0×10^{27} m^{-3}. (a) Fracture surface showing overall morphology and interaction layer. (b) Regions of high fission gas bubble density interspersed with regions which have no visible fission gas bubbles. (c) Polished and etched surface showing pattern of gas bubble growth. (d) Higher-magnification image of area in (c), showing gas bubble-free regions inside of cells.

decomposition toward fine-grained equilibrium $\alpha + \gamma'$ phases (Fig. 1) as a result of thermal exposure during the fabrication process. The quantity of the fine-grained regions containing α-U increases as the molybdenum content decreases. This complex microstructure presents opportunities for heterogeneous nucleation of gas bub-

Table 4
Measured fission gas bubble volume at 70% burnup

Fuel composition	Fission gas bubble volume fraction[a]
U–10Mo atomized	0.057
U–10Mo filings	0.095
U–8Mo	0.11
U–6Mo	0.12
U–4Mo	0.24

[a] Fraction of the unreacted regions of irradiated fuel particles.

bles at defect sites as well as in the high-swelling α-phase [34]. The presence of two distinct microstructural regions in the pre-irradiation microstructure presumably leads to two different mechanisms for fission gas bubble nucleation, resulting in two distinct gas bubble populations and fracture morphologies within a single fuel particle. One region consists of a flat fracture surface and a population of large bubbles, the other, a granular fracture surface with a distribution of finer bubbles. The granular structure is nearly identical to those found in high-burnup U_3O_8 dispersion fuel [35]. This type of microstructure has also been observed more recently in UO_2 power reactor fuel and is referred to as the 'rim effect' [36]. Grain refinement in these fuels is thought to be due to the accumulation of irradiation (fission) induced dislocations that eventually leads to recrystallization.

Evidence that the absence of pre-existing defects and chemical inhomogeneity retards the nucleation and growth of fission gas bubbles in U–Mo irradiated at low temperatures is shown in Fig. 13. The fuel particles shown in Fig. 13 are U–10Mo filings that were annealed at 1073 K for 50 h prior to fabrication into aluminum matrix fuel specimens [37]. The pre-irradiation microstructure of the annealed U–10Mo consists of fuel particles with regular grains; grain boundaries are visible on the etched specimen shown in Fig. 13(a). A few particles are in the midst of (thermally induced) recrystallization. Relative to the untreated fuel filings, a very low density of small fission gas bubbles form on irradiation to 2.6×10^{27} fissions m^{-3} (37.7 % ^{235}U burnup) at approximately 200 °C (Fig. 13(b)). It can be seen from Fig. 13(c) that by annealing out defect structures due to mechanical strain as well as small-scale chemical inhomogeneity, a very low population density of visible fission gas bubbles develop in the pattern of pre-irradiation grain boundaries.

A further example of the effect of pre-irradiation microstructure on fuel behavior at a fixed composition is provided by examination of U–10Mo atomized fuel particles and comparison of these with the U–10Mo filings. Prior to irradiation, the atomized fuel has a microstructure composed of a few primary grains of size

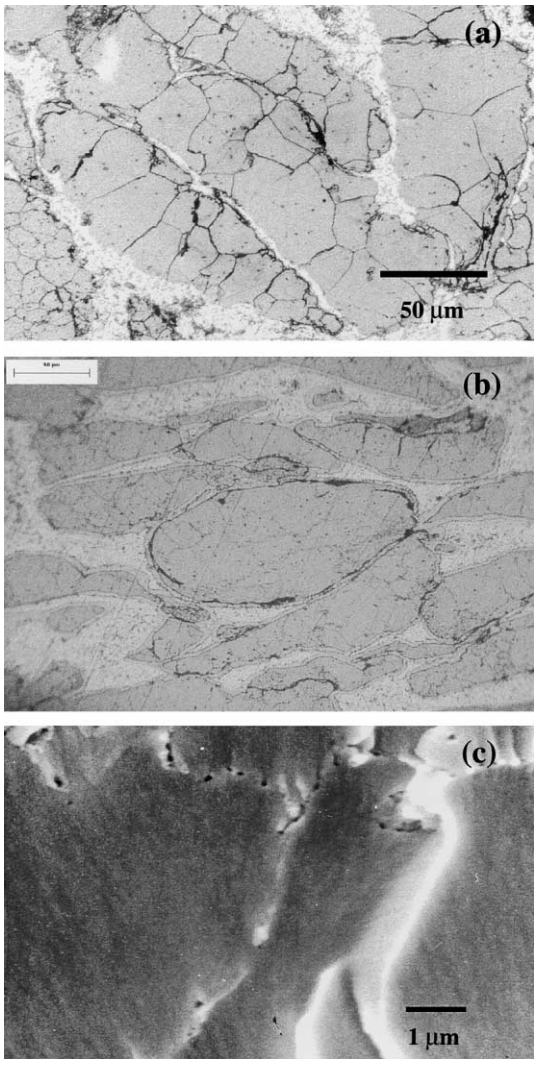

Fig. 13. U–10Mo fuel particles annealed at 800 °C prior to irradiation. (a) As-fabricated fuel microstructure. (b) Optical micrograph of polished surface after irradiation to 2.6×10^{27} fissions m^{-3} (37.7% burnup) at approximately 200 °C. (c) SEM fractograph showing low fission gas bubble population.

10–50 μm. The interior of the primary grains consists of a cored, cellular microstructure, with at least two compositionally distinct γ-(U,Mo) phases present [28]. Cell size is typically 2–5 μm. Nucleation of fission gas bubbles within the atomized fuel particles occurs first on the primary grain boundaries. Gas bubbles are also present in association with the lower molybdenum content γ-(U,Mo) phase present at the periphery of the cells. It thus appears that fission gas bubble nucleation is a function of molybdenum content in γ-(U,Mo) alloys. Overall, the concentration of crystal structure defects, such as dislocations and grain boundaries, is much lower

in the atomized fuel. The lower concentration of fission gas bubbles in the less defected material is consistent with the behavior of the annealed particles discussed above.

The fission gas behavior in U–4Mo fuel particles differed from that of the higher-alloy fuels. U–4Mo contained a population of large bubbles and exhibited evidence of bubble coarsening and linkup. This behavior in other fuels [6,7] precedes breakaway swelling; it is likely that U–4Mo would also exhibit this behavior on irradiation to higher burnup.

It is interesting to note that in the range of neutron flux and temperatures experienced by the fuel in these experiments, it is known that equilibrium $\alpha + \gamma'$ ($\gamma' = U_2Mo$) structures with sufficient alloy content (>5 wt% molybdenum) to be quenched into the metastable γ-phase will revert to the γ-phase on irradiation at low burnup [38,39]. It has been proposed that this phenomenon is related to rapid, localized heating and cooling cycles due to fission spikes, the net effect being a local heat and quench cycle. The presence or absence of this phenomenon could not be established in the current experiment, and potential effects on fuel behavior could not be gauged. Further experiments are planned to determine if phase-reversion is operative, and if it plays a role in fuel behavior.

5.2. Fuel–matrix interaction

Qualitative wavelength dispersive spectroscopy measurements indicate that the interaction layer that forms on irradiation contains all three of the major component elements of the fuel – U, Mo, and Al. It is apparent from inspection of the interaction layers that the reaction product performs well under irradiation. Apart from isolated instances, fission gas bubble growth is not observed in the interaction layer. The overall appearance after irradiation is similar to that of UAl_x-based fuel [40,41]. The volume change on stoichiometric conversion of U–6Mo to (U–6Mo)Al_3 is 8.6%, assuming a density of 6500 kg/m^3 for the reaction product. This amount of swelling on reaction is acceptable, since the layer grew uniformly during irradiation, with no void formation. The chief concern with excessive fuel–aluminum interaction is the depletion of the aluminum matrix material. This leads to a decrease in fuel meat thermal conductivity resulting in a rise in fuel centerline temperature. Due to the large amount of uranium alloy available for reaction in these very-high-density fuels, complete aluminum depletion can occur by reaction with the fuel phase.

Measurements of the thickness of the fuel–aluminum interaction layer as a function of burnup were taken from both SEM and optical micrographs. Flat regions of the fracture surface were compared to optical and SEM images of polished sections to obtain a reaction layer thickness. Since such measurements are skewed to larger values by oblique sectioning angles, a 'common minimum' value of interaction layer thickness was established. Measured interaction layer thickness for U–xMo fuels irradiated in RERTR-1 and 2 are plotted in Fig. 14 as a function of fuel particle fission density. The interaction layer growth rate for U–10Mo and U–8Mo is approximately the same. There was not a significant difference in the interaction layer thickness between U–10Mo atomized particles and U–10Mo filings. As the molybdenum content falls to 6 wt%, there is a definite increase in layer thickness at high burnup. The trend of increasing interaction rate continues for the 4 wt% molybdenum specimen. Parabolic layer growth kinetics are expected based on classical diffusion theory [42], and parabolic trend lines are drawn in Fig. 14 for high and low alloy compositions.

Out-of-pile thermal compatibility studies have shown this same trend of increasing fuel/aluminum reaction with decreasing molybdenum content [43]. In these tests, the increase in the rate of interaction was associated with the decomposition of metastable γ-phase fuel particles. Alloys with lower molybdenum alloy levels decompose faster, and the uranium/aluminum reaction proceeds more rapidly in these fuels. Penetration of aluminum into fuel particles occurred through cells of the non-gamma phase. The interaction zone was non-uniform, and 'kernels' of aluminide formed within the interior of fuel particles. This is in contrast to the uniform interaction layer found on the irradiated fuel particles (Fig. 9), and implies a different reaction mechanism during irradiation. The uniform interaction zone thickness suggests that classic irradiation-enhanced interdiffusion of a single phase alloy with aluminum is responsible for interaction layer growth during irradiation, and

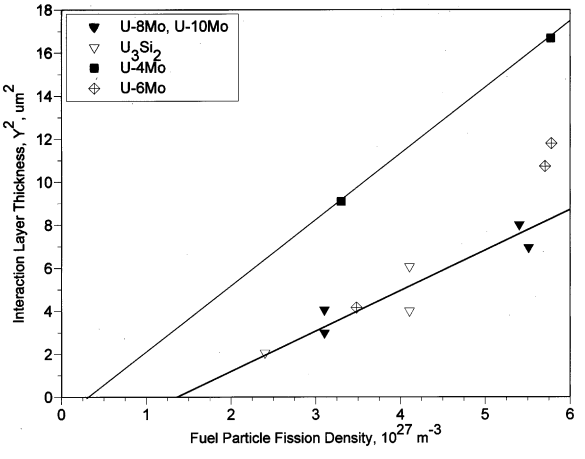

Fig. 14. Fuel/matrix interaction layer thickness for U–Mo fuels and U_3S_2 as a function of fission density.

that the interdiffusion rate is a function of molybdenum content.

6. Conclusion

Irradiation testing has been conducted on series of aluminum matrix U–Mo dispersion fuels. These fuels were irradiated to a maximum burnup of 70% ^{235}U at a temperature of approximately 65 °C. Fuels with 6 wt% or more molybdenum content performed well during irradiation, exhibiting low to moderate fuel/matrix interaction and stable fission gas bubble growth.

Fuel specimens containing U–6Mo, U–8Mo, and U–10Mo particles produced by filing have a similar process history and particle morphology. Fission gas-driven fuel particle swelling decreased in these fuels as alloy content increased from 6 to 10 wt%, as indicated by decreased gas bubble volume. The rate of fuel–matrix interaction increased when the molybdenum content was less than 8 wt%. The rate of interaction layer thickness increase was approximately the same for both U–10Mo atomized powder and fuel filings of the same composition. A larger volume of reaction product is formed in fuel made with U–10Mo filings owing to the higher surface-to-volume ratio relative to the atomized powder. The pre-irradiation microstructural state of the fuel particles was found to affect fission gas behavior within the fuel particles during irradiation. Fuel particles with the same composition (U–10Mo), but differing microstructures showed clear differences in fission gas behavior.

Fuel particles containing 4 wt% molybdenum reacted extensively with the matrix aluminum during fuel fabrication and irradiation. U–4Mo showed the growth of large fission gas bubbles by interlinking of smaller bubbles and extensive fuel–matrix interaction leading to interparticle contact. These behaviors increase the likelihood for the occurrence of breakaway swelling. Due to the more rapid reaction with aluminum and indications of unstable fission gas bubble growth, U–4Mo cannot be recommended as a fuel phase for dispersion in aluminum, although this alloy is attractive due to its high uranium density.

Acknowledgements

Special thanks are due to Dr Chang-Kyu Kim and his staff at KAERI for providing atomized powder for this experiment. The authors wish to acknowledge the assistance of R.W. Bratt, N.L. Dietz, S.M. Frank, P.A. Hansen, W. Kettman, D.J. McGann, I.G. Prokofiev, J.D. Rule, and R.L. Taylor for experimental work. The authors also wish to acknowledge Fred Ingram, Gray Chang, and Richard Ambrosek of the ATR at INEEL for their contributions in irradiation testing.

References

[1] 10CFR50, Limiting the use of highly enriched uranium in domestically licensed research reactors, Federal Register, vol. 51, no. 377, 1986.
[2] J.L. Snelgrove, G.L. Hofman, M.K. Meyer, C.L. Trybus, T.C. Wiencek, Nucl. Eng. Des. 178 (1997) 119.
[3] J.P. Durand, Y. Lavastre, M. Grasse, in: Proceedings of the 20th International Meeting on Reduced Enrichment for Research and Test Reactors, Argonne National Laboratory Report ANL/TD/TM99-06, 1999, p. 28.
[4] H.B. Peacock, Coextrusion of 60 to 30 wt% U_3O_8 Nuclear Fuel Elements, DPST-80-447, E.I. du Pont de Nemours and Company, 1980.
[5] M. Ugajin, A. Itoh, M. Akabori, N. Ooka, Y. Nakakura, J. Nucl. Mater. 254 (1998) 78.
[6] M.K. Meyer, T.C. Wiencek, S.L. Hayes, G.L. Hofman, J. Nucl. Mater. 278 (2000) 358.
[7] G.L. Hofman, R.F. Domagala, G.L. Copel, J. Nucl. Mater. 150 (1987) 238.
[8] G. Beghi, Gamma Phase Uranium-Molybdenum Fuel Alloys, EUR 5053e, Euratom, 1968.
[9] D.E. Thomas, R.H. Fillnow, K.M. Goldman, J. Hino, R.J. Van Thyne, F.C. Holtz, D.J. McPherson, in: Proceedings of the Second UN International Conference on the Peaceful Uses of Atomic Energy, 5 P/1924 UN, Geneva, 1958.
[10] C.W. Dean, A study of the time–temperature-transformation behavior of a uranium–7.5 weight percent niobium–2.5 weight percent zirconium alloy, in: Oak Ridge Y-12 Plant Report ORNL Y-1694, 1969.
[11] M.M. Karnowsky, R.E. Rohde, J. Nucl. Mater. 49 (1973–1974) 81.
[12] F. Giraud-Heaud, J. Guillaumin, Acta Metall. 21 (1973) 1243.
[13] R.A. Vandermeer, in: J.J. Burke, D.A. Colling, A.E. Gorum, J. Greenspan (Eds.), Physical Metallurgy of Uranium Alloys, Brook Hill, 1976, p. 219.
[14] M.K. Meyer, G.L. Hofman, T.C. Wiencek, S.L. Hayes, J.L. Snelgrove, J. Nucl. Mater. 299 (2001) 175.
[15] C.L. Trybus, T.C. Wiencek, M.K. Meyer, D.J. McGann, C.R. Clark, in: Proceedings of the 20th International Meeting on Reduced Enrichment for Research and Test Reactors, Argonne National Laboratory Report ANL/TD/TM99-06, 1999, p. 19.
[16] K.-H. Kim, D.B. Lee, C.-K. Kim, I.H. Kuk, K.W. Paik, J. Nucl. Sci. Technol. 34 (1997) 1127.
[17] T.C. Wiencek, Summary Report on Fuel Development and Miniplate Fabrication for the RERTR Program, 1978 to 1990, Argonne National Laboratory Report ANL/RERTR/TM-15, 1995.
[18] M.K. Meyer, C.L. Trybus, G.L. Hofman, S.M. Frank, T.C. Wiencek, in: Proceedings of the 1997 International Meeting on Reduced Enrichment for Research and Test Reactors, Argonne National Laboratory Report ANL/TD/TM99-06, 1999, p. 81.

[19] H.L. Yackel, in: J.J. Burke, D.A. Colling, A.E. Gorum, J. Greenspan (Eds.), Physical Metallurgy of Uranium Alloys, Brook Hill, 1976, p. 259.
[20] P.E. Repas, R.H. Goodenow, R.F. Hehemann, Trans. Am. Soc. Met. 57 (1964) 150.
[21] R.F. Hills, D.R. Harries, D.J. Hodkin, M.B. Waldron, Transformation of Metastable Phases in the Uranium-Molybdenum Alloy System, AERA M/R 2840, UK Atomic Energy Agency, Harwell, 1959.
[22] R.K. McGeary, Development and Properties of Uranium-Base Alloys Resistant in High Temperature Water, WAPD-127, part I, US Atomic Energy Commission Report, 1955.
[23] R.J. Van Thyne, D.J. McPherson, Trans. ASM 49 (1957) 598.
[24] Y. Goldstein, A. Bar-Or, J. Inst. Met. 95 (1967) 17.
[25] J. Lehmann, R.F. Hills, J. Nucl. Mater. 10 (1960) 261.
[26] G.L. Hofman, J.L. Snelgrove, in: R.W. Cahn, P. Haasen, E.J. Kramer (Eds.), Materials Science and Technology, vol. 10A, VCH, New York, 1994, p. 45 (Chapter 2).
[27] K.H. Kim, D.B. Lee, C.K. Kim, G.L. Hofman, K.W. Paik, Nucl. Eng. Des. 178 (1997) 111.
[28] B.-S. Seong, C.-H. Lee, J.-S. Lee, H.S. Shim, J.-H. Lee, K.-H. Kim, C.K. Kim, V. Em, J. Nucl. Mater. 277 (2000) 274.
[29] S.L. Hayes, C.L. Trybus, M.K. Meyer, in: Proceedings of the 1997 International Meeting on Reduced Enrichment for Research and Test Reactors, Argonne National Laboratory Report ANL/TD/TM-99-06, 1999, p. 190.
[30] M.L. Griebenow, G.H. Hansen, A.P. Larrick, EG&G Report RE-A-77-059, 1977.
[31] D.R. Olander, Fundamental Aspects of Nuclear Reactor Fuel Elements, US Energy Research and Development Administration Report TID-26711-P1, 1976.
[32] M.P. Johnson, W.A. Holland, Irradiation of U–Mo base Alloys, Atomics International/North American Aviation Report NAA-SR-6262, 1964.
[33] A.A. Shoudy, W.E. McHugh, M.A. Silliman, in: Radiation Damage in Reactor Materials, IAEA, Vienna, 1962, p. 133.
[34] J. Rest, G.L. Hofman, I. Konovalov, A. Maslov, Proceedings of the 1998 International Meeting on Reduced Enrichment for Research and Test Reactors, Sao Paulo, Brazil, October 18–23, in press.
[35] G.L. Hofman, J. Rest, J.L. Snelgrove, in: Proceedings of the 19th International Meeting on Reduced Enrichment for Research and Test Reactors, Korea Atomic Energy Research Institute Report, 1996, p. 202.
[36] L.E. Thomas, C.E. Beyer, L.A. Chariot, J. Nucl. Mater. 188 (1992) 80.
[37] S.L. Hayes, M.K. Meyer, C.R. Clark, J.R. Stuart, I.G. Prokofiev, T.C. Wiencek, Proceedings of the 1999 International Meeting on Reduced Enrichment for Research and Test Reactors, Budapest, Hungary, 3–8 October 1999, in press.
[38] M.L. Bleiberg, L.J. Jones, B. Lustman, J. Appl. Phys. 27 (1956) 1270.
[39] M.L. Bleiberg, J. Nucl. Mater. 2 (1959) 182.
[40] J. Gómez, R. Morando, E.E. Perez, D.R. Giorsetri, G.L. Copeland, G.L. Hofinan, J.L. Snelgrove, in: Proceedings of the 1984 International Meeting on Reduced Enrichment for Research and Test Reactors, Argonne, IL, Argonne National Laboratory Report ANL/RERTR/TM-6, 1985, p. 86.
[41] W. Dienst, S. Nazare, F. Thummler, J. Nucl. Mater. 64 (1977) 1.
[42] J. Rest, in: Proceedings of the 2000 International Meeting on Reduced Enrichment for Research and Test Reactors, Las Vegas, NV, Argonne National Laboratory Report ANL/TD/TM01-12, 2001, p. 159.
[43] D.B. Lee, K.H. Kim, C.K. Kim, J. Nucl. Mater. 250 (1997) 79.